NANO LETTERS

pubs.acs.org/NanoLett Letter

Super-Resolution Raman Scattering Imaging Enabled by Rough Metal Films

Hongki Lee, Ming Lei, Junxiang Zhao, Guanghao Chen, Jie Hu, Zachary Burns, Fanglin Tian, and Zhaowei Liu*

Cite This: *Nano Lett.* 2025, 25, 8954−8960 Read Online

ACCESS | Metrics & More | Article Recommendations | Supporting Information

ABSTRACT: A super-resolution Raman scattering microscopy technique is demonstrated by combining localized surface plasmon-based structured illumination microscopy with the blindSIM algorithm. This approach enables super-resolution Raman scattering imaging of dielectric nanoparticles with sub-100 nm resolution. The technique leverages the surface-enhanced Raman scattering effect of rough silver films to generate near-field speckle patterns, enabling subdiffraction-limited optical sampling and enhanced Raman signals. The method demonstrates the excitation/emission modulation between emitters separated by subdiffraction distances. Experimental results reveal that background subtraction for Raman images from polystyrene beads generates image contrasts predominantly consisting of Raman-shifted photons. The enhanced signal-to-noise ratio obtained from 80 nm polystyrene beads proves sufficient for applying the blindSIM algorithm. The result presents a remarkable resolution enhancement, surpassing the diffraction limit by 4.4 times and successfully resolving 80 nm dielectric nanoparticles. This approach represents a significant advancement in label-free super-resolution imaging, offering potential applications in various fields of microscopy and materials science.

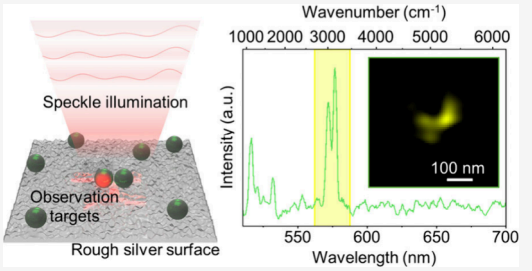

KEYWORDS: *label-free imaging, Raman scattering microscopy, super-resolution imaging, structured illumination microscopy, localized surface plasmon*

Label-free imaging has emerged as a crucial technique in the field of optical microscopy, offering valuable insights into biological specimens and novel materials without the need for fluorescent labeling.[1,2] This approach leverages the intrinsic properties of light, such as phase,[3] polarization,[4] nonlinearity,[5] inelastic scattering,[6,7] and infrared absorption,[8,9] to provide both qualitative and quantitative analysis of samples in their native state. Among the various label-free imaging techniques, Raman microscopy has made significant strides in achieving superior chemical imaging.[10−14] By leveraging the inelastic scattering of light, Raman microscopy enables the visualization of molecular vibrations, offering a wealth of chemical information about the sample. The field has seen significant advances through techniques such as stimulated Raman scattering and coherent anti-Stokes Raman scattering, which substantially enhance sensitivity and image contrast compared to the traditional spontaneous Raman scattering microscopy.[15−20]

Inspired by advancements in super-resolution fluorescence microscopy, researchers have applied similar principles to Raman imaging to achieve a better resolution in Raman scattering images. One such approach is the adaptation of structured illumination microscopy (SIM) techniques.[21,22] SIM is based on exciting specimens using spatially structured patterns of light. The fundamental principle involves mixing the spatial frequency of the object and illumination pattern to make unresolvable information observable. Regular SIM uses known illumination structures, with gratings, and has been shown to double the resolution of spontaneous Raman scattering microscopy.[23,24] Meanwhile, for cases where the illumination pattern is unknown, the blindSIM algorithm has demonstrated the super-resolution reconstruction in optical imaging.[25,26] In the far-field regime, both SIM and blindSIM typically achieve a 2-fold resolution enhancement, which is the theoretical limit for linear SIM due to the diffraction limit. To further push the boundaries of resolution enhancement in linear response systems, researchers have turned to deep subwavelength structured illumination with plasmonic and metamaterial nanostructures. Techniques such as localized surface plasmon (LSP) based SIM and hyperbolic metamaterial based SIM have demonstrated significant improvements in fluorescence imaging and scattering imaging in resolution beyond the 2-fold limit of conventional SIM.[27−32]

Received: February 18, 2025
Revised: May 16, 2025
Accepted: May 21, 2025
Published: May 22, 2025

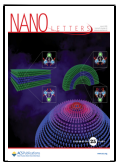

https://doi.org/10.1021/acs.nanolett.5c01083
Nano Lett. 2025, 25, 8954−8960

In this study, we combine an LSP-based SIM scheme with the blindSIM algorithm to showcase resolution enhancement in Raman scattering imaging. This approach not only benefits from the super-resolution capabilities of LSP-based SIM but also harnesses the surface-enhanced Raman scattering (SERS) effect to amplify the intensity of Raman signals.[33,34] Spontaneous Raman scattering and SERS is considered an incoherent process because the scattered photons from individual molecules within a sample have no fixed phase relationship with each other, making it well-suited for blindSIM algorithm.[35,36] While similar approaches have been explored in previous studies,[24,37−40] there has been a notable gap in demonstrating reconstructed images of neighboring separate nanoparticles less than 100 nm apart. Our research addresses this limitation by utilizing the localized near-fields of a rough silver surface to generate super-resolution images of neighboring dielectric nanoparticles.

Plasmonic metallic films exploit the interaction between an incident light and local electron oscillations, allowing them to convey spatial frequency components of light beyond those supported in free space.[41] As shown in Figure 1a, the near-field

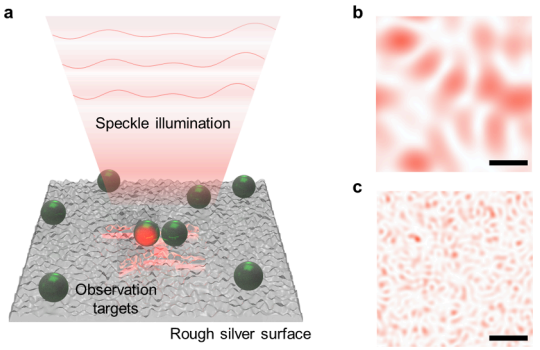

Figure 1. Working principle of near-field speckle based label-free super-resolution imaging. (a) Schematic representation of near-field speckle generation on a rough silver surface. (b) Exemplary speckle patterns (E-field) produced by diffraction-limited far-field light. (c) Exemplary speckle patterns (E-field) generated by localized near-fields. The scale bar is 500 nm.

speckles produced by the interaction between incident light and the nanoscale roughness of silver films exhibit enhanced local field intensities and spatial confinement compared to far-field speckles, making them valuable for imaging applications. The distribution of high-resolution speckle patterns can be modulated by varying the incident angles and directions. While speckle patterns formed by the diffraction-limited far-field light have a maximum wavevector of k_0 ($k_0 = 2\pi/\lambda$ in free space) as shown in Figure 1b, they can transform into near-field speckle patterns via scattering from the random roughened silver nanostructures, which supports higher-k modes. These higher-k modes help shift the object's high spatial frequency information into the observable k-space, overcoming the conventional SIM resolution limit of 2-fold improvement. Figure 1c demonstrates exemplary speckle patterns which are generated with higher wavevectors than k_0 at a wavelength of 488 nm.

To demonstrate near-field speckle generation on the rough silver film, we examine the morphology of a rough silver film and perform finite element method calculations using COMSOL Multiphysics, as illustrated in Figure 2 (details in the Supporting Information). Figure 2a displays the atomic force microscopy image of a rough silver film, revealing a maximum height variation of approximately 15 nm. The observed surface roughness and grains correspond to the typical size of LSP modes on silver nanoparticles, which is crucial for generating near-field speckles. The localized near-fields of LSP modes in silver surface typically occur in the 5−60 nm range, aligning with the film's surface features.[42] In our simulation, far-field speckle patterns are used to illuminate the rough silver film surface, efficiently inducing near-field speckles.[28] By simulating the illumination of far-field speckle patterns on the rough silver surface, the model captures the excitation of LSP and the generation of near-field speckles. The incident polarization is defined as TM-polarized (transverse magnetic). The model obtains multiple electric field distributions under varying illumination conditions, specifically different polar (θ) and azimuthal (φ) angles. The far-field speckles can be generated by the superposition of electric fields having random phase variables ψ_i at different φ_i and θ_i, described as

$$E_{speckle}(x, y, z) = \sum_{i=1}^{N} A_i E_{\phi_i,\theta_i}(x, y, z)\exp(i\psi_i) \quad (1)$$

N is the total number of plane waves used in the superposition. $E_{\phi_i,\theta_i}(x, y, z)$ is a plane wave propagating along k_x, k_y, and k_z with given θ and φ. A_i is the amplitude of each plane wave. ψ_i is a random phase term uniformly distributed between 0 and 2π. The random phase term ψ_i plays a vital role in enabling dynamic variation of near-field speckles, eliminating the need for complex illumination optics to achieve different θ and φ, which simplifies the overall system design and implementation. Examples of such far-field speckle patterns are shown in the insets of Figure 2b,c. Similarly, the near-field distribution resulting from the random far-field speckle illuminations can be obtained in the evanescent field region of the rough silver film, as depicted in Figure 2b,c. The lateral near-field distributions shown in Figure 2b,c are calculated at a distance of 20 nm from the rough silver surface.

Here, two key characteristics of the near-field speckles contribute to the reconstruction of super-resolution Raman scattering images: near-field enhancement and subdiffraction limited optical sampling by localized near-fields. The simulation shows a near-field amplification of $|E_{max}/E_{in}| \sim 5$ as demonstrated by two near-field distributions in Figure 2b,c. Figure 2d illustrates the electric field profiles of the rough silver film from the distributions in Figure 2b,c. The rough silver surface generates higher wavevector light components than those in the air, supporting LSP modes and surface plasmon polariton (SPP) modes on the surface. Such light components enable higher spatial sampling with subdiffraction limited excitation of Raman-active molecules. In Figure 2d, this effect is demonstrated by the sharper near-field peaks near the rough surface, where dashed lines represent the E-field amplitude profiles of near-field speckles and dotted lines represent those of far-field speckles. Near-field speckles possess a broadband wavevector spectrum, combining diffraction-limited speckles and plasmon-induced speckles. The presence of high spatial frequency wavevectors from SPPs and LSPs can also be confirmed via a two-dimensional Fourier transform of the near-field intensity distribution, as shown in Figure S1. These high-frequency components can shift fine spatial details of the sample into the detectable passband, effectively enhancing the imaging resolution. From the comparison in Figure S1c, the

https://doi.org/10.1021/acs.nanolett.5c01083
Nano Lett. 2025, 25, 8954−8960

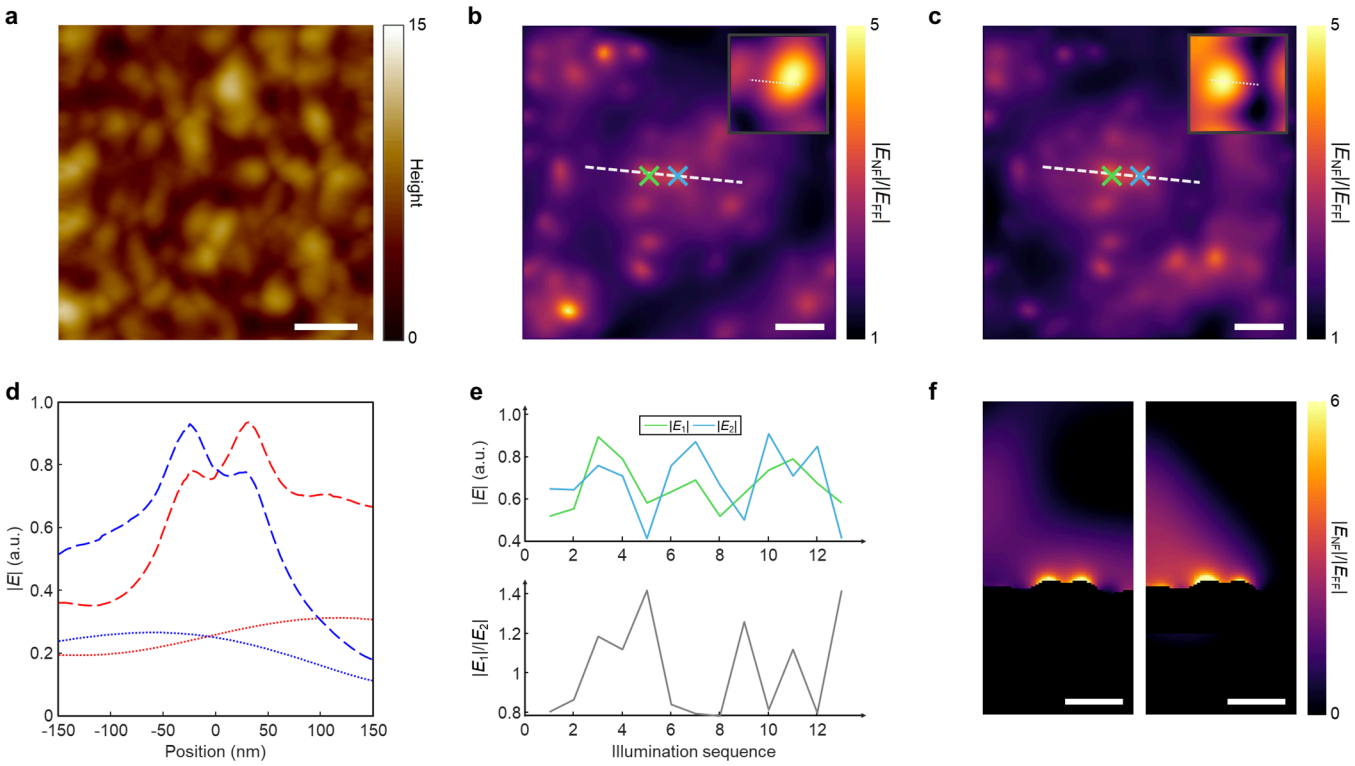

Figure 2. Characterization of near-field speckle generation. (a) An atomic force microscopy image of a rough silver film. (b, c) Examples of near-field speckle generation under different far-field incident illumination sequences. The comparison between near-field (E_{NF}) and far-field (E_{FF}) electric fields illustrates the amplification. The insets show the corresponding far-field speckles used to illuminate the silver film. (d) Electric field profiles of different near-filed speckles in (b) (blue) and (c) (red). Dashed lines represent the profiles of near-field speckles while dotted lines represent those of far-field speckles. (e) The field variations during the illumination sequence at two different positions marked by green and blue crosses in (b, c). The near-field speckles in (b, c) correspond to the third and tenth illuminations, respectively. (f) Side views of the near-field speckles in (b, c). The scale bars are 100 nm.

plasmonic effects from the rough silver film are expected to boost the resolution compared to conventional diffraction-limited techniques. In addition, rough silver films further improve the image contrast through enhanced light emission near the rough surface, attributed to both increased local density of optical states and mirror effects.[43] Those phenomena collectively amplify the Raman emission from the molecules near the surface, improving the contrast and sensitivity of the Raman imaging.

For successful super-resolution image reconstruction using the blindSIM algorithm, emitters separated by subdiffraction distances must exhibit sufficient excitation/emission contrast to preserve detailed real-space information. Figure 2e investigates the fluctuation of localized near-fields $|E|$ at two points separated by 50 nm, denoted by blue and green crosses in Figure 2b. The ratio between the two points can differ by up to 40%, providing sufficient image contrasts for the Raman-shifted photon emission for blindSIM image reconstruction. Figure 2f illustrates the near-field distribution in xz space. Figure S2 also shows the field enhancement profile at the green cross point along the z direction. The field enhancement directly on the surface is calculated to be 5.9, while at distances above 200 nm, beyond the evanescent wave region, the field enhancement becomes negligible at unity.

To experimentally demonstrate the amplified Raman signals on the silver film, we test the wide-field Raman imaging of polystyrene beads on a randomly roughened silver substrate (details in the Supporting Information). A 100 nm thick silver film is used, sufficiently thick to block background fluorescence from the glass substrate. Initially, an aqueous suspension of 200 nm polystyrene beads is dropped-cast onto the rough silver film surface and air-dried. The beads are observed on the silver film using a 100× objective lens with NA = 0.9 and a 2.5× magnifier. A single 200 nm bead is confirmed through dark-field imaging, as shown in Figure 3a, with an EMCCD camera (pixel size is 64 nm). A continuous-wave 488 nm laser is used for illumination, coupled with a mechanically vibrating multimode fiber which generates far-field speckle patterns. By correlating the positions of two wide-field images from the EMCCD camera and the spectrometer camera (pixel size is 175 nm), we obtain the Raman spectrum of a 200 nm polystyrene bead, as shown in Figure 3b. The major Raman peaks observed for polystyrene include C−O stretching modes (1026 cm^{-1}), aromatic C = C stretching vibrations (1450 cm^{-1}), CH_2 asymmetric and symmetric stretching vibrations (2800−2950 cm^{-1}), and aromatic C−H symmetric stretching vibrations (3000−3100 cm^{-1}).[44] Ten frames are averaged to produce each Stokes-shifted image in Figure 3c,d.

In Figure 3b, the fluorescent background is removed using polynomial background subtraction.[45] Raman scattering images of polystyrene, shown in Figure 3c, primarily capture the vibrational modes from CH_2 asymmetric and symmetric stretching and aromatic C−H symmetric stretching using a bandpass filter centered at 575 nm with a 25 nm bandwidth. Background subtraction is also applied to the Raman scattering image in Figure 3c. The ratio between Raman-shifted photons and background photons (I_{Raman}/I_{BG}) is calculated in both the spectral and spatial domains. In the spectral domain, I_{Raman}/I_{BG}

https://doi.org/10.1021/acs.nanolett.5c01083
Nano Lett. 2025, 25, 8954−8960

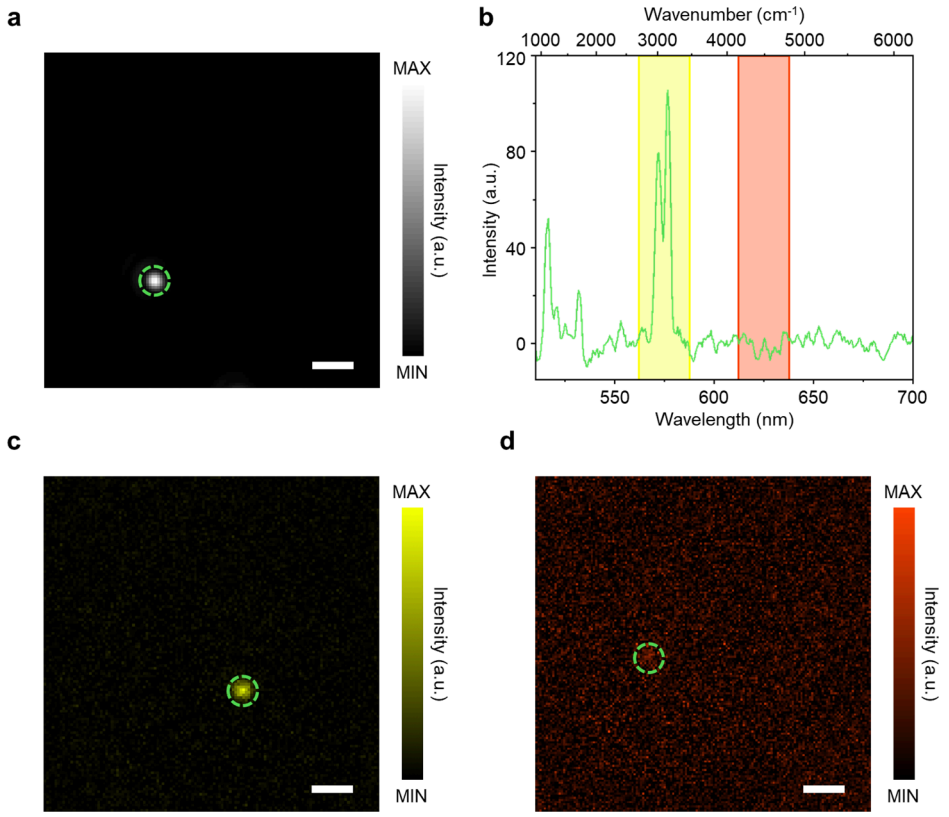

Figure 3. SERS images of 200 nm polystyrene beads on rough silver films. (a) A dark-field image of a single polystyrene 200 nm bead. (b) A SERS spectrum from the same bead which is shown in (a). (c) A wide-field SERS image using an optical filter centered at 575 nm with a 25 nm bandwidth which captures the Raman-shifted photons from the vibrational modes from CH_2 asymmetric and symmetric stretching vibrations and aromatic C−H symmetric stretching vibrations, as highlighted in the yellow box in (b). (d) A wide-field image using an optical filter at 625 nm with a 26 nm bandwidth which captures only the non-Raman-shifted photons, as highlighted in the red box in (b). The same polystyrene bead is observed in all the images. The scale bar is 1 μm.

is determined to be 0.13, where the spectral intensity of a single bead is integrated from 562.5 to 587.5 nm (observation area = 525 × 700 nm^2). From the wide-field image, I_{Raman}/I_{BG} is calculated to be 13.42, where I_{Raman} is chosen from the peak intensity pixel in Figure 3c. The values obtained from both domains indicate that the silver surface is the primary source of background signal, influencing the signal-to-background ratio. To verify that background fluorescence does not contribute to the image obtained with the bandpass filter in Figure 3c, an off-Raman scattering image is acquired, as shown in Figure 3d. This image is captured using a different bandpass filter centered at 625 nm with a 26 nm bandwidth. The off-Raman scattering image reveals that only negligible scattering of fluorescence lights from the silver surface by the polystyrene bead is observed. This result confirms that the Raman scattering image in Figure 3c, after background subtraction, predominantly consists of Raman-shifted photons.

In Figure 3c, the signal-to-noise ratio (SNR) of the wide-field Raman scattering image of the 200 nm polystyrene bead is measured to be 27. When the bead is illuminated by the near-field speckle, as detailed in Figure S3, two distinct volume regions with different light intensities can be identified: one where the evanescent field dominates, and another where the far-field speckle is predominant. Assuming an evanescent field depth of 20 nm into the dielectric nanoparticle, with an average field intensity enhancement of 12, the total electric energy within the 200 nm diameter polystyrene bead's volume can be obtained as $T_{200} = 0.5 \times \int \epsilon |E|^2 dV \propto I_{inc} \times 5.5 \times 10^6$ J. This calculation considers both the evanescent and far-field contributions to the overall field intensity. Considering the particle volume and the near-field illumination volume, we can estimate the SNR for smaller nanoparticles. For instance, for an 80 nm polystyrene bead, the total electric energy within its volume can be obtained as $T_{80} = 0.5 \times \int \epsilon |E|^2 dV \propto I_{inc} \times 7.3 \times 10^5$ J. Assuming the background fluorescence (primarily from the silver surface) remains constant, the expected SNR for the 80 nm polystyrene bead would be approximately 3.6, calculated as $T_{80}/T_{200} \times 27$. This SNR will be sufficient for applying the blindSIM algorithm to produce super-resolution Raman scattering images.[29] Figure S4 demonstrates the case of super-resolution image reconstruction of 200 nm beads using a bandpass filter centered at 575 nm, which surpasses the theoretical optical resolution of the system (575 nm/(2 × 0.9) =319 nm) by 1.6 times.

Here, we apply the same image acquisition and reconstruction method to the Raman scattering imaging of the polystyrene beads having a diameter of 80 nm. As denoted, the continuous-wave laser light at 488 nm is illuminated with mechanically vibrating multimode fiber, which generates the far-field speckle pattern. The exposure time is set to be 1 s, with 3 accumulations. As in the case of 200 nm polystyrene beads, CH_2 asymmetric and symmetric stretching vibrations and aromatic C−H symmetric stretching vibrations are observed using the same band-pass filter. Prior to scanning electron microscopy (SEM) imaging (which requires additional metallic coating), the bead aggregation is excited by

https://doi.org/10.1021/acs.nanolett.5c01083
Nano Lett. 2025, 25, 8954−8960

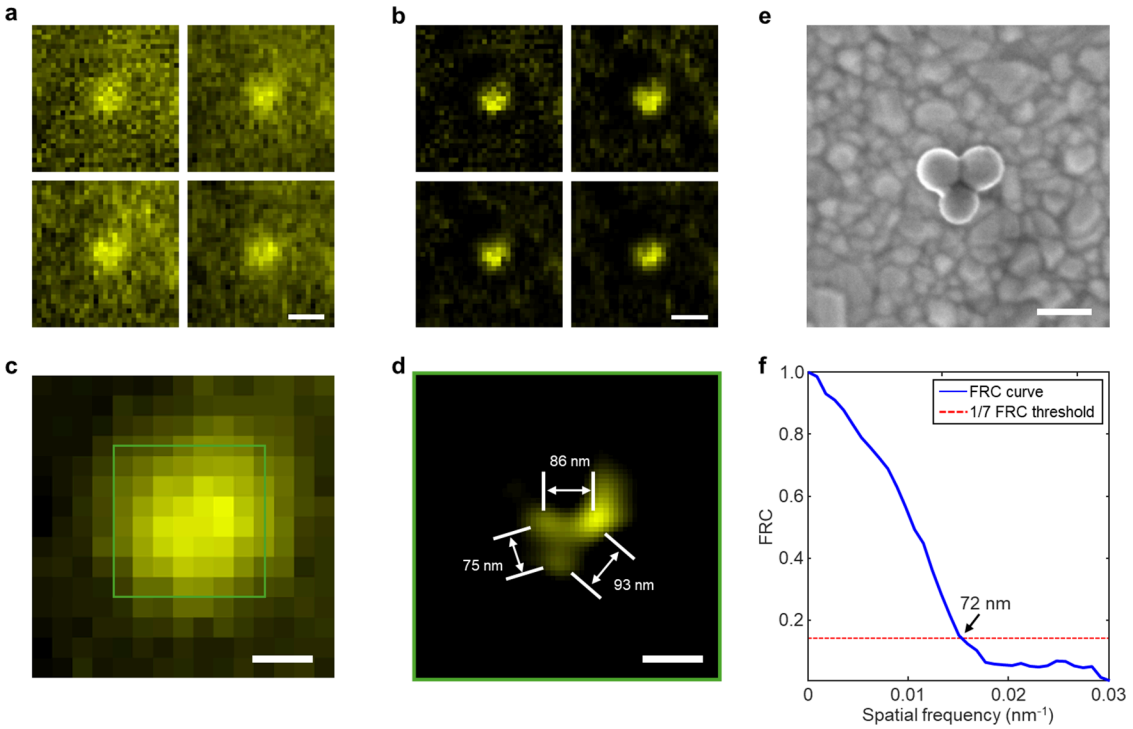

Figure 4. Super-resolved SERS images of 80 nm polystyrene beads on rough silver films. (a) Examples of raw Raman scattering images of aggregated 80 nm polystyrene beads obtained by near-field speckle illumination. (b) Deconvolved Raman scattering images in (a). (c) Integration of the raw Raman scattering images of aggregated 80 nm polystyrene beads by near-field speckle illumination. (d) Super-resolution reconstruction of Raman scattering image of 80 nm polystyrene beads. (e) SEM image of the same 80 nm polystyrene beads observed in (d). (f) The Fourier ring correlation analysis of reconstructed Raman scattering image. The standard 1/7 FRC resolution criterion is used where a 72 nm Fourier space cutoff is shown. Scale bars in (a, b), (c), and (d, e) are 500, 200, and 100 nm, respectively.

random near-field speckle illuminations. A series of 13 frames (total acquisition time: 39 s) with high SNR are used as subframes for blindSIM image reconstruction, as described in Figure 4a. The image SNR of the aggregated 80 nm beads in subframes is measured to be 9.03 ± 2.15. Through iterative deconvolution, the blindSIM algorithm effectively processes low-SNR images. Figure 4b shows examples of removing background fluorescence in the Raman-shifted subframe images by the deconvolution process for each frame. The background fluorescence is clearly removed, which as a result generates the improved SNR of 19.46 ± 3.62. Figure 4c shows the integration of raw diffraction-limited Raman-shifted images at the center wavelength of 575 nm, while Figure 4d presents the super-resolution reconstruction. In contrast to the blurred diffraction-limited image, the reconstruction clearly resolves three individual beads, which is in good agreement with the SEM image in Figure 4e which is taken after the optical measurement. To validate the resolution attained, we also employ Fourier ring correlation (FRC) analysis, a widely recognized resolution criterion in super-resolution microscopy.[46] Applying the standard 1/7 FRC resolution criterion to two reconstruction images, we demonstrate an achieved resolution of 72 nm as shown in Figure 4f. This result represents a remarkable enhancement in spatial resolution, surpassing the diffraction limit by more than 4.4 folds. Figure S5 shows an additional case of super-resolution reconstruction for 80 nm beads having different separation distances. Notably, while two beads are in contact, the third is separated by 122 and 118 nm from the others, respectively, which is consistent with the SEM results. These reconstruction results confirm the capability of our method to resolve subdiffraction features in Raman imaging with high fidelity.

In conclusion, we have successfully demonstrated sub-100 nm resolution in label-free SERS-based near-field speckle imaging, beyond the diffraction limit. This achievement represents the first demonstration of resolving neighboring dielectric nanoparticles separated by 80 nm for Raman scattering microscopy. Our approach utilizes a simple scheme with rough silver films as a plasmonic substrate, proving the concept's viability and potential for further development. While LSP modes are primarily governed by the local metal-dielectric geometry, controlling individual LSPs becomes increasingly difficult when adjacent geometries are in close proximity due to plasmonic coupling. Thus, simply reducing the surface random roughness does not guarantee improved resolution, which is a limitation of LSP-based SIM. Several avenues for optimization and improvement exist. Achieving more uniform and stronger near-field amplification, as well as higher wavevector generation, could further improve both sensitivity and resolution.[28,47] Addressing potential thermal issues by incorporating heat sink mechanisms could also improve the stability and reliability of the imaging process.[48] Furthermore, implementing advanced reconstruction techniques has the potential to significantly enhance both reconstruction speed and resolution.[49] By pursuing these optimizations, we can further refine and expand the capabilities of this label-free super-resolution imaging technique.

https://doi.org/10.1021/acs.nanolett.5c01083
Nano Lett. 2025, 25, 8954−8960

■ ASSOCIATED CONTENT

Supporting Information

The Supporting Information is available free of charge at https://pubs.acs.org/doi/10.1021/acs.nanolett.5c01083.

Detailed information about the numerical model and method, sample preparation, experimental setup, high spatial frequency wavevectors of SPPs and LSPs, an axial field enhancement profile, near-field and far-field illuminations of dielectric nanoparticles, super-resolution image reconstruction of 200 nm beads, and super-resolved SERS images of 80 nm polystyrene beads on rough silver films (PDF)

■ AUTHOR INFORMATION

Corresponding Author

Zhaowei Liu − *Department of Electrical and Computer Engineering, University of California, San Diego, California 92093, United States;* orcid.org/0000-0002-5732-8109; Email: zhaowei@ucsd.edu

Authors

Hongki Lee − *Department of Electrical and Computer Engineering, University of California, San Diego, California 92093, United States;* orcid.org/0000-0002-0655-1925

Ming Lei − *Department of Electrical and Computer Engineering, University of California, San Diego, California 92093, United States;* orcid.org/0000-0001-6687-9044

Junxiang Zhao − *Department of Electrical and Computer Engineering, University of California, San Diego, California 92093, United States*

Guanghao Chen − *Department of Electrical and Computer Engineering, University of California, San Diego, California 92093, United States*

Jie Hu − *Department of Electrical and Computer Engineering, University of California, San Diego, California 92093, United States*

Zachary Burns − *Department of Electrical and Computer Engineering, University of California, San Diego, California 92093, United States*

Fanglin Tian − *Department of Electrical and Computer Engineering, University of California, San Diego, California 92093, United States*

Complete contact information is available at: https://pubs.acs.org/10.1021/acs.nanolett.5c01083

Author Contributions

H.L. conducted the theoretical analysis and the experiment. M.L. and F.T. fabricated rough silver films. J.Z., G.C., and J.H. helped during the experimental work. J.Z. and Z.B. contributed to the image reconstruction process. Z.L. supervised the work. H.L. and Z.L. wrote the manuscript.

Notes

The authors declare no competing financial interest.

■ ACKNOWLEDGMENTS

This work was partially supported by the National Science Foundation (Grant no. ECCS-2320437). This work was performed in part at the San Diego Nanotechnology Infrastructure (SDNI) of UCSD, a member of the National Nanotechnology Coordinated Infrastructure, which is supported by the National Science Foundation (Grant no. ECCS-2025752). Hongki Lee's work was partially supported by the Basic Science Research Program through the National Research Foundation of Korea (NRF) funded by the Ministry of Education (Grant no. NRF-RS-2023-00245748).

■ REFERENCES

(1) Shaked, N. T.; Boppart, S. A.; Wang, L. H. V.; Popp, J. Label-free biomedical optical imaging. *Nat. Photonics* **2023**, *17* (12), 1031−1041.

(2) Raghunathan, R.; Vasquez, M.; Zhang, K.; Zhao, H.; Wong, S. T. C. Label-free optical imaging for brain cancer assessment. *Trends Cancer* **2024**, *10* (6), 557−570.

(3) Park, Y.; Depeursinge, C.; Popescu, G. Quantitative phase imaging in biomedicine. *Nat. Photonics* **2018**, *12* (10), 578−589.

(4) Yeh, L. H.; Ivanov, I. E.; Chandler, T.; Byrum, J. R.; Chhun, B. B.; Guo, S. M.; Foltz, C.; Hashemi, E.; Perez-Bermejo, J. A.; Wang, H. J.; Yu, Y. H.; Kazansky, P. G.; Conklin, B. R.; Han, M. H.; Mehta, S. B. Permittivity tensor imaging: modular label-free imaging of 3D dry mass and 3D orientation at high resolution. *Nat. Methods* **2024**, *21* (7), 1257−1274.

(5) Tu, H. H.; Liu, Y.; Marjanovic, M.; Chaney, E. J.; You, S. X.; Zhao, Y. B.; Boppart, S. A. Concurrence of extracellular vesicle enrichment and metabolic switch visualized label-free in the tumor microenvironment. *Sci. Adv.* **2017**, *3* (1), No. e1600675.

(6) Okada, M.; Smith, N. I.; Palonpon, A. F.; Endo, H.; Kawata, S.; Sodeoka, M.; Fujita, K. Label-free Raman observation of cytochrome c dynamics during apoptosis. *Proc. Natl. Acad. Sci. U. S. A.* **2012**, *109* (1), 28−32.

(7) Tabata, K.; Kawagoe, H.; Taylor, J. N.; Mochizuki, K.; Kubo, T.; Clement, J. E.; Kumamoto, Y.; Harada, Y.; Nakamura, A.; Fujita, K.; Komatsuzaki, T. On-the-fly Raman microscopy guaranteeing the accuracy of discrimination. *Proc. Natl. Acad. Sci. U. S. A.* **2024**, *121* (12), No. e2304866121.

(8) Ishigane, G.; Toda, K.; Tamamitsu, M.; Shimada, H.; Badarla, V. R.; Ideguchi, T. Label-free mid-infrared photothermal live-cell imaging beyond video rate. *Light sci. appl.* **2023**, *12* (1), 174.

(9) Bai, Y. R.; Yin, J. Z.; Cheng, J. X. Bond-selective imaging by optically sensing the mid-infrared photothermal effect. *Sci. Adv.* **2021**, *7* (20), No. eabg1559.

(10) Cheng, J. X.; Xie, X. S. Vibrational spectroscopic imaging of living systems: An emerging platform for biology and medicine. *Science* **2015**, *350* (6264), aaa8870.

(11) Wei, L.; Yu, Y.; Shen, Y.; Wang, M. C.; Min, W. Vibrational imaging of newly synthesized proteins in live cells by stimulated Raman scattering microscopy. *Proc. Natl. Acad. Sci. U. S. A.* **2013**, *110* (28), 11226−11231.

(12) Lu, F. K.; Basu, S.; Igras, V.; Hoang, M. P.; Ji, M.; Fu, D.; Holtom, G. R.; Neel, V. A.; Freudiger, C. W.; Fisher, D. E.; Xie, X. S. Label-free DNA imaging in vivo with stimulated Raman scattering microscopy. *Proc. Natl. Acad. Sci. U. S. A.* **2015**, *112* (37), 11624−11629.

(13) Evans, C. L.; Potma, E. O.; Puoris'haag, M.; Cote, D.; Lin, C. P.; Xie, X. S. Chemical imaging of tissue in vivo with video-rate coherent anti-Stokes Raman scattering microscopy. *Proc. Natl. Acad. Sci. U. S. A.* **2005**, *102* (46), 16807−16812.

(14) Freudiger, C. W.; Min, W.; Saar, B. G.; Lu, S.; Holtom, G. R.; He, C. W.; Tsai, J. C.; Kang, J. X.; Xie, X. S. Label-free biomedical imaging with high sensitivity by stimulated Raman scattering microscopy. *Science* **2008**, *322* (5909), 1857−1861.

(15) Prince, R. C.; Frontiera, R. R.; Potma, E. O. Stimulated Raman Scattering: From Bulk to Nano. *Chem. Rev.* **2017**, *117* (7), 5070−5094.

(16) Oh, S.; Lee, C.; Yang, W.; Li, A.; Mukherjee, A.; Basan, M.; Ran, C.; Yin, W.; Tabin, C. J.; Fu, D.; Xie, X. S.; Kirschner, M. W. Protein and lipid mass concentration measurement in tissues by stimulated Raman scattering microscopy. *Proc. Natl. Acad. Sci. U. S. A.* **2022**, *119* (17), No. e2117938119.

(17) Gong, L.; Zheng, W.; Ma, Y.; Huang, Z. W. Higher-order coherent anti-Stokes Raman scattering microscopy realizes label-free

super-resolution vibrational imaging. *Nat. Photonics* **2020**, *14* (2), 115−122.
(18) Zhang, W. X.; Li, Y. J.; Fung, A. A.; Li, Z.; Jang, H.; Zha, H. H.; Chen, X. P.; Gao, F. Y.; Wu, J. Y.; Sheng, H. X.; Yao, J. J.; Skowronska-Krawczyk, D.; Jain, S.; Shi, L. Y. Multi-molecular hyperspectral PRM-SRS microscopy. *Nat. Commun.* **2024**, *15* (1), 1599.
(19) Wang, W. Q.; Huang, Z. W. Stimulated Raman scattering microscopy with phase-controlled light focusing and aberration correction for rapid and label-free, volumetric deep tissue imaging. *Opto-Electron. Adv.* **2024**, *7* (9), 240064.
(20) Bi, S. M.; Li, Y. M.; Ao, J. P.; Liu, Z. J.; Weng, M. L.; Ji, M. B. On-Chip Stimulated Raman Scattering Imaging and Quantification of Molecular Diffusion in Aqueous Microfluidics. *Anal. Chem.* **2025**, *97* (4), 2052−2061.
(21) Gustafsson, M. G. Surpassing the lateral resolution limit by a factor of two using structured illumination microscopy. *J. Microsc.* **2000**, *198*, 82−87.
(22) Frohn, J. T.; Knapp, H. F.; Stemmer, A. True optical resolution beyond the Rayleigh limit achieved by standing wave illumination. *Proc. Natl. Acad. Sci. U. S. A.* **2000**, *97* (13), 7232−7236.
(23) Watanabe, K.; Palonpon, A. F.; Smith, N. I.; Chiu, L. D.; Kasai, A.; Hashimoto, H.; Kawata, S.; Fujita, K. Structured line illumination Raman microscopy. *Nat. Commun.* **2015**, *6*, 10095.
(24) Wang, M. Q.; Zhang, C. L.; Yan, S.; Chen, T.; Fang, H.; Yuan, X. C. Wide-Field Super-Resolved Raman Imaging of Carbon Materials. *ACS Photonics* **2021**, *8* (6), 1801−1809.
(25) Mudry, E.; Belkebir, K.; Girard, J.; Savatier, J.; Le Moal, E.; Nicoletti, C.; Allain, M.; Sentenac, A. Structured illumination microscopy using unknown speckle patterns. *Nat. Photonics* **2012**, *6* (5), 312−315.
(26) Guilbert, J.; Negash, A.; Labouesse, S.; Gigan, S.; Sentenac, A.; de Aguiar, H. B. Label-free super-resolution stimulated Raman scattering imaging of biomedical specimens. *Adv. Imaging* **2024**, *1*, 011004.
(27) Bezryadina, A.; Zhao, J.; Xia, Y.; Zhang, X.; Liu, Z. High spatiotemporal resolution imaging with localized plasmonic structured illumination microscopy. *ACS Nano* **2018**, *12* (8), 8248.
(28) Lee, Y. U.; Zhao, J.; Ma, Q.; Khorashad, L. K.; Posner, C.; Li, G.; Wisna, G. B. M.; Burns, Z.; Zhang, J.; Liu, Z. Metamaterial assisted illumination nanoscopy via random super-resolution speckles. *Nat. Commun.* **2021**, *12* (1), 1559.
(29) Lee, Y. U.; Li, S.; Wisna, G. B. M.; Zhao, J.; Zeng, Y.; Tao, A. R.; Liu, Z. Hyperbolic material enhanced scattering nanoscopy for label-free super-resolution imaging. *Nat. Commun.* **2022**, *13* (1), 6631.
(30) Lee, H.; Yoo, H.; Moon, G.; Toh, K. A.; Mochizuki, K.; Fujita, K.; Kim, D. Super-resolved Raman microscopy using random structured light illumination: Concept and feasibility. *J. Chem. Phys.* **2021**, *155* (14), 144202.
(31) Yoo, H.; Lee, H.; Rhee, W. J.; Moon, G.; Lee, C.; Lee, S. A.; Shin, J. S.; Kim, D. Disordered Nanocomposite Islands for Nanospeckle Illumination Microscopy in Wide-Field Super-Resolution Imaging. *Adv. Opt. Mater.* **2021**, *9* (15), 2100211.
(32) Liu, X. Z.; Kong, W. J.; Wang, C. T.; Pu, M. B.; Li, Z. Y.; Yuan, D.; Li, X.; Ma, X. L.; Luo, X. G. Hyperbolic metamaterial-assisted structured illumination microscopy using periodic sub- diffraction speckles. *Opt. Mater. Express* **2022**, *12* (8), 3108−3117.
(33) Fu, M.; Mota, M. P. D. P.; Xiao, X. F.; Jacassi, A.; Gusken, N. A.; Chen, Y. X.; Xiao, H. F.; Li, Y.; Riaz, A.; Maier, S. A.; Oulton, R. F. Near-unity Raman beta-factor of surface-enhanced Raman scattering in a waveguide. *Nat. Nanotechnol.* **2022**, *17* (12), 1251−1257.
(34) Ma, H.; Pan, S. Q.; Wang, W. L.; Yue, X. X.; Xi, X. H.; Yan, S.; Wu, D. Y.; Wang, X.; Liu, G. K.; Ren, B. Surface-Enhanced Raman Spectroscopy: Current Understanding, Challenges, and Opportunities. *ACS Nano* **2024**, *18* (22), 14000−14019.
(35) Liebel, M.; Pazos-Perez, N.; van Hulst, N. F.; Alvarez-Puebla, R. A. Surface-enhanced Raman scattering holography. *Nat. Nanotechnol.* **2020**, *15* (12), 1005−1011.
(36) Vento, V.; Velez, S. T.; Pogrebna, A.; Galland, C. Measurement-induced collective vibrational quantum coherence under spontaneous Raman scattering in a liquid. *Nat. Commun.* **2023**, *14* (1), 2818.
(37) Olson, A. P.; Ertsgaard, C. T.; Elliott, S. N.; Lindquist, N. C. Super-resolution chemical imaging with plasmonic substrates. *ACS Photonics* **2016**, *3* (3), 329−336.
(38) Olson, A. P.; Spies, K. B.; Browning, A. C.; Soneral, P. A. G.; Lindquist, N. C. Chemically imaging bacteria with super-resolution SERS on ultra-thin silver substrates. *Sci. Rep.* **2017**, *7*, 9135.
(39) Lee, H.; Kang, K.; Mochizuki, K.; Lee, C.; Toh, K. A.; Lee, S. A.; Fujita, K.; Kim, D. Surface plasmon localization-based super-resolved Raman microscopy. *Nano Lett.* **2020**, *20* (12), 8951−8958.
(40) Ertsgaard, C. T.; McKoskey, R. M.; Rich, I. S.; Lindquist, N. C. Dynamic placement of plasmonic hotspots for super-resolution surface-enhanced Raman scattering. *ACS Nano* **2014**, *8* (10), 10941−10946.
(41) Raether, H. *Surface plasmon on smooth and rough surface and on gratings*; Springer: Verlag, 1988.
(42) Liang, Y. Z.; Li, L. X.; Lu, M. D.; Yuan, H. Z.; Long, Z. W.; Peng, W.; Xu, T. Comparative investigation of sensing behaviors between gap and lattice plasmon modes in a metallic nanoring array. *Nanoscale* **2018**, *10* (2), 548−555.
(43) Klantsataya, E.; François, A.; Ebendorff-Heidepriem, H.; Sciacca, B.; Zuber, A.; Monro, T. M. Effect of surface roughness on metal enhanced fluorescence in planar substrates and optical fibers. *Opt. Mater. Express* **2016**, *6* (6), 2128−2138.
(44) Boronat, C.; Correcher, V.; García-Guinea, J.; Bravo-Yagüe, J. C. Effects of UVC irradiation on polystyrene for healthcare packaging: Study by FTIR and Raman spectroscopy with thermoluminescence. *Polym. Degrad. Stab.* **2024**, *222*, 110700.
(45) Zhao, J.; Lui, H.; McLean, D. I.; Zeng, H. Automated autofluorescence background subtraction algorithm for biomedical Raman spectroscopy. *Appl. Spectrosc.* **2007**, *61* (11), 1225−1232.
(46) Nieuwenhuizen, R. P. J.; Lidke, K. A.; Bates, M.; Puig, D. L.; Grünwald, D.; Stallinga, S.; Rieger, B. Measuring image resolution in optical nanoscopy. *Nat. Methods* **2013**, *10* (6), 557−562.
(47) Shen, H.; Chen, L.; Ferrari, L.; Lin, M. H.; Mortensen, N. A.; Gwo, S.; Liu, Z. Optical observation of plasmonic nonlocal effects in a 2D superlattice of ultrasmall gold nanoparticles. *Nano Lett.* **2017**, *17* (4), 2234−2239.
(48) Wang, K.; Schonbrun, E.; Steinvurzel, P.; Crozier, K. B. Trapping and rotating nanoparticles using a plasmonic nano-tweezer with an integrated heat sink. *Nat. Commun.* **2011**, *2*, 469.
(49) Burns, Z.; Liu, Z. W. Untrained, physics-informed neural networks for structured illumination microscopy. *Opt. Express* **2023**, *31* (5), 8714−8724.

https://doi.org/10.1021/acs.nanolett.5c01083
Nano Lett. 2025, 25, 8954−8960